Title
Noncovalent π-stacked robust topological organic framework

Journal
Proceedings of the National Academy of Sciences of the United States of America, 117(34)

ISSN
0027-8424

Authors
Meng, Dong
Yang, Jonathan Lee
Xiao, Chengyi
et al.

Publication Date
2020-08-25

DOI
10.1073/pnas.2010733117

Peer reviewed

Noncovalent π-stacked robust topological organic framework

Dong Meng[a,b,1], Jonathan Lee Yang[c,1], Chengyi Xiao[d], Rui Wang[a,b], Xiaofei Xing[e], Olkan Kocak[f], Gulsevim Aydin[f], Ilhan Yavuz[f], Selbi Nuryyeva[g], Lei Zhang[d], Guogang Liu[h], Zhenxing Li[a,b,e,2], Shuai Yuan[i], Zhao-Kui Wang[i], Wei Wei[j], Zhaohui Wang[h], K. N. Houk[g,2], and Yang Yang[a,b,2]

[a]Department of Materials Science and Engineering, University of California, Los Angeles, CA 90095; [b]California NanoSystems Institute, University of California, Los Angeles, CA 90095; [c]Department of Chemistry, University of California, Berkeley, CA 94720; [d]Beijing Advanced Innovation Center for Soft Matter Science and Engineering, Beijing University of Chemical Technology, 100029 Beijing, China; [e]State Key Laboratory of Heavy Oil Processing, College of New Energy and Materials, China University of Petroleum (Beijing), 102249 Beijing, China; [f]Department of Physics, Marmara University, 34722 Istanbul, Turkey; [g]Department of Chemistry and Biochemistry, University of California, Los Angeles, CA 90095; [h]Key Laboratory of Organic Optoelectronics and Molecular Engineering, Department of Chemistry, Tsinghua University, 100084 Beijing, China; [i]Institute of Functional Nano & Soft Materials (FUNSOM), Jiangsu Key Laboratory for Carbon-Based Functional Materials & Devices, Soochow University, 215123 Suzhou, China; and [j]Department of Chemistry, Capital Normal University, 100048 Beijing, China

Contributed by K. N. Houk, June 27, 2020 (sent for review May 28, 2020; reviewed by Hongjie Dai and Zhiyong Tang)

Organic frameworks (OFs) offer a novel strategy for assembling organic semiconductors into robust networks that facilitate transport, especially the covalent organic frameworks (COFs). However, poor electrical conductivity through covalent bonds and insolubility of COFs limit their practical applications in organic electronics. It is known that the two-dimensional intralayer π···π transfer dominates transport in organic semiconductors. However, because of extremely labile inherent features of noncovalent π···π interaction, direct construction of robust frameworks via noncovalent π···π interaction is a difficult task. Toward this goal, we report a robust noncovalent π···π interaction-stacked organic framework, namely πOF, consisting of a permanent three-dimensional porous structure that is held together by pure intralayer noncovalent π···π interactions. The elaborate porous structure, with a 1.69-nm supramaximal micropore, is composed of fully conjugated rigid aromatic tetragonal-disphenoid-shaped molecules with four identical platforms. πOF shows excellent thermostability and high recyclability and exhibits self-healing properties by which the parent porosity is recovered upon solvent annealing at room temperature. Taking advantage of the long-range π···π interaction, we demonstrate remarkable transport properties of πOF in an organic-field-effect transistor, and the mobility displays relative superiority over the traditional COFs. These promising results position πOF in a direction toward porous and yet conductive materials for high-performance organic electronics.

COFs | field-effect transistor | organic conductor

The rise of organic semiconductors has sparked development of flexible displays (1–3), organic solar cells (4–7), sensors (8–10), and optical devices (11–13). Aside from low cost, one of the most striking properties of organic electronic materials is their adjustability via facile chemical modifications to different device requirements. Advanced computational and experimental tools have been developed to provide insights into the structure–property relationship in organic semiconductors and consequently predict their electronic properties. However, controlled large-scale assembly is one of the more crucial aspects for effective charge transport in organic semiconductors and is difficult to achieve. The emergence of organic frameworks (OFs) has opened an avenue for predicting and controlling the molecular assembly, especially in covalent OFs (COFs) (14–17). The final COF topology can now be determined based on the relative geometries of raw materials. However, poor electrical conductivity of covalent bonds and insolubility of COF still limit their practical applications in organic electronics. Moreover, the irreversibility of covalent bonds deprives COF of the possibility for self-healing using simple methods.

It is well known that the transport along the π···π network in a two-dimensional (2D) in-plane direction is considered to be a key transport mechanism in organic semiconductors, which would lay the foundation for a high-performing device. Furthermore, the noncovalent π···π interaction is easily repairable with a simple heat treatment due to the interaction's "soft" property. However, because of the inherent features of noncovalent π···π interactions (weak, flexible, and poor directionality), direct construction of porous framework with a permanent porosity is challenging, as the structure will most likely collapse after solvent removal and decompose upon heating. Hence, pure intralayer noncovalent π···π interaction-constructed porous materials with an ordered structure arouse special interest. In this study, we achieve this material by increasing the π plane and enhancing the effective overlapping area by intermolecular linking forces for a stable framework. Also, the directional face-on packing of the end group and the geometry of the middle core yield a robust material with precise and predictable control (18–23).

Significance

A robust noncovalent π···π interaction-stacked organic framework (OF), called πOF, consisting of a permanent three-dimensional porous structure that is held together by pure intralayer noncovalent π···π interactions is synthesized and characterized. πOF shows excellent thermostability and high recyclability and exhibits self-healing properties by which the parent porosity is recovered upon solvent annealing at room temperature. We demonstrate remarkable transport properties of πOF in an organic-field-effect transistor, with mobility that is superior to traditional covalent OFs. πOF is a porous and conductive material for high-performance organic electronics.

Author contributions: D.M. and Y.Y. designed research; D.M., J.L.Y., C.X., R.W., X.X., O.K., G.A., I.Y., S.N., L.Z., G.L., Z.L., S.Y., Z.-K.W., W.W., Z.W., and K.N.H. performed research; D.M., K.N.H., and Y.Y. wrote the paper; D.M. and Y.Y. conceived the concept; D.M. and J.L.Y. synthesized the molecule, grew the crystals, and performed structural characterization; C.X., R.W., L.Z., S.Y., and Z.-K.W. fabricated the OFET devices; O.K., G.A., I.Y., S.N., and K.N.H. performed and analyzed the computations; G.L. and Z.W. performed the crystal characterization; X.X. and Z.L. performed the sorption experiments; and W.W. refined the single-crystal structure.

Reviewers: H.D., Stanford University; and Z.T., National Center for Nanoscience and Technology.

The authors declare no competing interest.

[1]D.M. and J.L.Y. contributed equally to this work.

[2]To whom correspondence may be addressed. Email: lizx@cup.edu.cn, houk@chem.ucla.edu, or yangy@ucla.edu.

This article contains supporting information online at https://www.pnas.org/lookup/suppl/doi:10.1073/pnas.2010733117/-/DCSupplemental.

First published August 11, 2020.

Here, we designed a three-dimensional (3D) organic framework, namely **πOF**, based on solely the noncovalent π···π interactions between **SFIC** molecules. This **SFIC** molecule uses a biplanar conjugated cruciform-shaped spirobifluorene (**SF**) as the centroid core and 3-(dicyanomethylidene)indan-1-one (**IC**) as a multijoint fragment connecting adjacent molecules, which exhibits a tetragonal-disphenoid-shaped molecular conformation and self-assembles into a 3D porous structure of **πOF**. Despite the extremely labile noncovalent π···π interactions, **πOF** exhibited not only supramaximal micropore (1.69 nm) and extremely high surface area (981.62 $m^2 \cdot g^{-1}$) but also high thermal stability and recyclability, as demonstrated by variable-temperature and recycling-test powder X-ray diffraction (PXRD) experiments. Moreover, after the heat treatment, **πOF** was able to self-heal and retrieve the parent porosity upon solvent annealing (methanol/chloroform) at room temperature. The activated powdered **πOF** exhibited high CO_2 and N_2 adsorption capacity due to its pore-rich structure. Interestingly, **πOF**-based organic-field-effect transistor (OFET) showed remarkable electron and hole transport abilities, which are attributed to abundant π···π interactions in the structure. Theoretical calculations predict anisotropy in charge mobilities; π···π stacking involves a strong transfer integral and both hole and electron mobilities are maximized in this transport direction. The nonlocal charge–phonon coupling critically affects the charge transport in **πOF**.

Results and Discussion

Synthesis and Molecular Assembly. The target monomer **SFIC** was obtained via Knoevenagel condensation between SF-CHO and 3-(dicyanomethylidene)indan-1-one (**IC**) in 90% yield (Fig. 1*A*). The structure was confirmed by ^{1}H NMR, ^{13}C NMR, and high-resolution mass spectrometry (*SI Appendix*). **SFIC** is soluble in common organic solvents such as dichloromethane, chloroform, chlorobenzene and *ortho*-dichlorobenzene at room temperature because of the cross-linked molecular scaffold and the branched alkyl chains. The thermal properties were evaluated using thermal gravimetric analysis under nitrogen. **SFIC** showed high thermal stability with 5% weight loss at decomposition temperature of over 351 °C (*SI Appendix*, Fig. S2). The bandgap was investigated by ultraviolet-visible spectrum and electrochemical cyclic voltammetry as shown in *SI Appendix*, Fig. S7 and Table S3. The optical bandgap obtained from the edge of absorption spectra in the film was calculated to be 1.75 eV. The energy level and electrochemical bandgap are estimated to be −5.77 eV for highest occupied molecular orbital (HOMO), −3.94 eV for lowest unoccupied molecular orbital (LUMO), and 1.83 eV for bandgap, which are obtained from the onset oxidation and reduction potentials and the difference of HOMO and LUMO, respectively. The narrow bandgap attributes to the strong electron withdrawing of end group IC and endows the system with ambipolar characteristics.

The molecular conformation of **SFIC**, which is a tetragonal-disphenoid shape, was confirmed by XRD analysis of single crystals obtained by slow vapor diffusion ($CHCl_3$/MeOH). The dimensions of **SFIC** conformer are ∼21.92 Å in length, ∼19.13 Å in width, and ∼14.28 Å in height (Fig. 1*B*). Two IC groups on the same wing are noncoplanar with a dihedral angle of 28.07°. Each criss-crossed **SFIC** molecule is connected to four adjacent **SFIC** molecules (which are rotated 90° relative to the centroid molecule) through four pairs of π···π interactions through antiparallel end groups (EGs) (Fig. 1*C*). Such packing forms a 2D reticular quadrangular array which undergoes perpendicular slipped one-dimensional (1D) stacking through two different types of CH···π interactions (Fig. 1*D* and *SI Appendix*, Fig. S4) of hexylbenzene side chains forming a final 3D lamellar structure. We confirmed that the orientation of **SFIC** molecules of adjacent 2D layers are identical and assemble into two repeating layers with a 3.94-Å-long unidirectional slippage (between two parallel wings, d_{sp}) and 5.57-Å-long bidirectional slippage (between two central carbon atoms, d_s) (Fig. 1*D*). Closer investigation of the structure reveals that four discrete **SFIC** molecules of each layer form a dimetric micropore, which has a diameter of 2.12 nm (Fig. 1*C*) across the layer and a lower diameter of 1.69 nm (Fig. 1*D*) between two layers due to the slippage of adjacent layers.

Investigation of Morphology and Sorption of SFIC-πOF. The rhomboid-shaped morphology of πOF with diagonal lengths of 50.5 μm and 59.5 μm was observed using transmission electron microscopy (TEM) (Fig. 2*A*), with the thickness of the crystal thinning toward the edges. The obvious crystal lattice fringes of πOF can be observed in the high-resolution TEM (HRTEM) image (Fig. 2*B*), demonstrating the high crystallinity of the prepared πOF. The lattice fringe was measured to be about 3.94 Å, which is identical to the unidirectional slippage distance between the two parallel wings of two **SFIC** molecules from adjacent layers (Fig. 2*C*).

As shown in Fig. 2*D*, the as-prepared **πOF** exhibited high CO_2 uptake capacity of 62.41 $cm^3 \cdot g^{-1}$ (blue line) due to its highly porous structure and weak basicity of cyano group in **SFIC**. Furthermore, the powdery sample of guest-free **πOF** presented a typical type I sorption isotherm for N_2 bearing a steep slope in the high relative pressure (P/P_0) range for microporous structure within the 1-to-2-nm range (Fig. 2*D*). The corresponding Brunauer–Emmett–Teller surface area was over 981.62 $m^2 \cdot g^{-1}$ (red line in Fig. 2*D*) and pore volume was 0.44 $cm^3 \cdot g^{-1}$. The pore size distribution of **πOF** based on the nonlocal density functional theory (NLDFT) model showed a single peak at 1.69 nm (Fig. 2*D*, *Inset*), which is consistent with the uniform dimetric pores of crystal packing structure. The elemental mapping images (Fig. 2*E*) displayed a highly uniform dispersion of C and N elements throughout the entire **πOF**. Porous material with supermicroporous range of 1 to 2 nm and higher surface area shown in this work is a significant achievement that will bridge the gap between mesoporous materials and microporous zeolites.

The porous crystals after activation, particularly when guest-free, are less stable than other porous materials that are linked by dynamic covalent bonds or metal coordination bonds, while some hydrogen-bonded porous crystals are able to keep the original crystal framework after the removal of guest molecules. Few of the nonclassical hydrogen-bond-constructed (C-H···X) porous crystals could survive beyond 130 °C (24, 25). Compared to conventional hydrogen bonds, and even the nonclassical ones, π···π interactions are far more labile. Surprisingly, our more-labile **πOF** based on **SFIC** is significantly more thermally robust than the reported hydrogen-bonded frameworks, showing no change up to 180 °C in variable-temperature PXRD patterns (Fig. 2*G*). The structure remained identical to that of the simulated one from the single-crystal structure, with peaks at $2\theta = 5.3°$, 9.2°, and 11.5° assigned to (020), (031), and (400) lattice planes. Upon heating to 200 °C and beyond, the PXRD patterns changed suddenly, indicating a transition into a different crystalline phase.

Self-healing materials have received tremendous attention recently (26–28). However, in the case of solid materials, presence of notable healing properties often results in low thermostability. **πOF**, on the other hand, showed excellent thermal stability with peaks maintaining themselves at temperatures of over 180 °C in variable-temperature PXRD (Fig. 2*G*). After heat treatment at 240 °C, **πOF** self-healed, retrieving its parent porosity upon solvent annealing (methanol/chloroform vapor) at room temperature (Fig. 2*I*), and the original diffraction peaks were completely recovered 24 h after solvent annealing and the intensity gradually increased with time (Fig. 2*H*). We also tested the recyclability of **πOF** using PXRD measurements. After every five cycles of N_2 adsorption, the PXRD of **πOF** was measured to examine the change in the original framework structure. **πOF** retained its original crystalline structure and

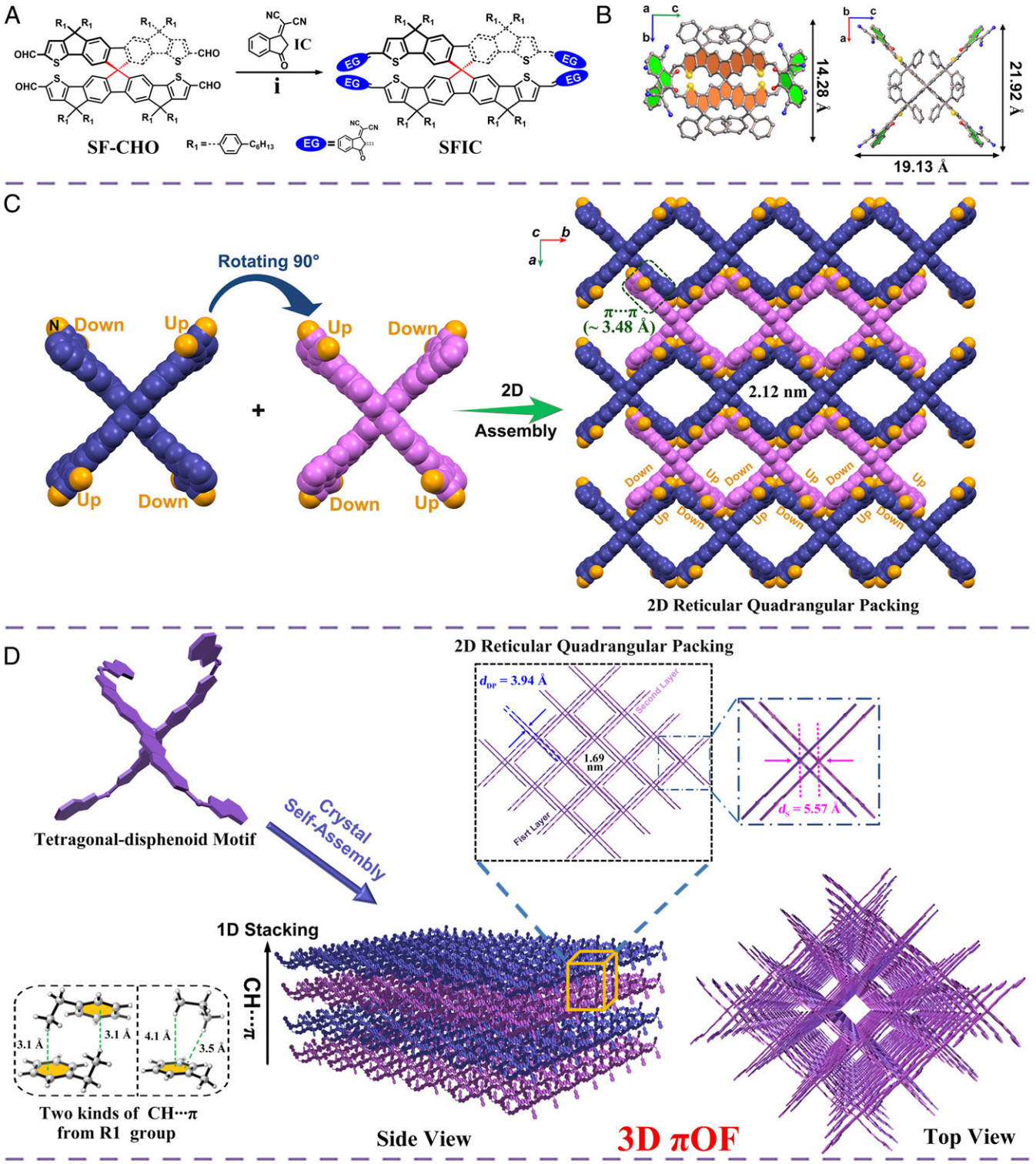

Fig. 1. Synthetic route and crystal packing arrangement. (*A*) Synthetic route with reaction conditions of (i) 3-(dicyanomethylidene)indan-1-one (IC, 12 equivalents) and pyridine (1 mL) in chloroform at 70 °C with yield of 90%. (*B*) The single-crystal X-ray molecular structure [top (*Left*) and side (*Right*) view] display a tetragonal-disphenoid motif. (*C*) The 2D crystal assembly along the *ac* plane via π···π interactions. The directions of up and down refer to the direction of the N atom. (*D*) The molecular packing arrangement of the 3D πOF structure is composed of 2D π···π (*ac* plane) interactions and 1D CH···π (*b* axis) interactions. d_{DP} and d_S stand for packing and slippage distances between layers, respectively. The alkyl chains, hydrogen and oxygen atoms, and cyano groups are omitted for clarity.

skeleton even after 30 cycles, as can be seen from the unaltered positions and strength of peaks in PXRD profiles (Fig. 2*F*). These results suggest that **πOF** is of admirable stability and is highly reusable, suggesting noteworthy self-healing ability.

Single-Crystal Transistor Characterization of SFIC-πOF. Owing to its long-range π···π interactions, **πOF** offers an opportunity to expand the OF into organic electronics. Hence, we first prepared the single-crystal microplates of **πOF** by a typical drop-casting

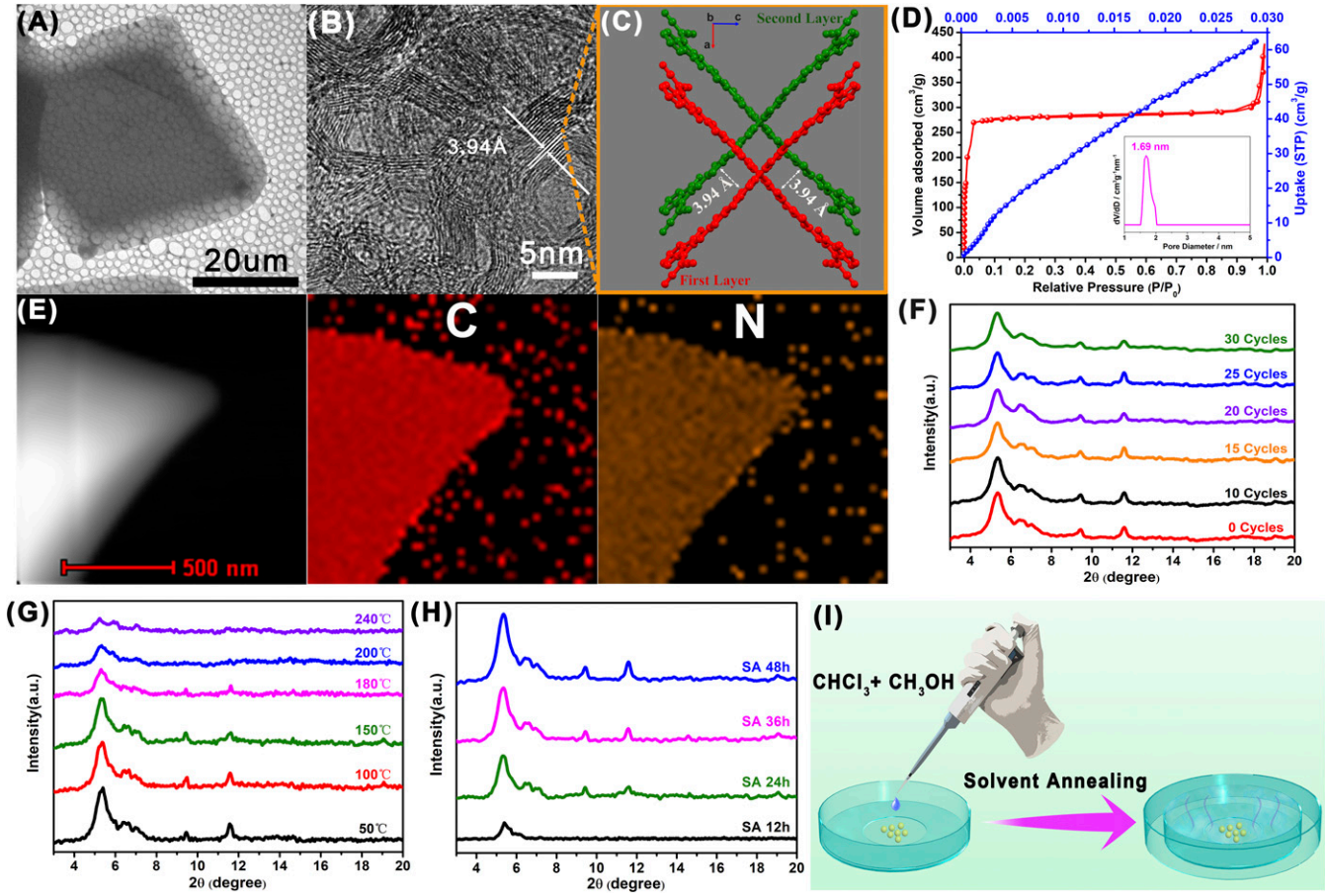

Fig. 2. The morphology and sorption characterizations of πOFs. (*A*) TEM image and (*B*) HRTEM image of πOF. (*C*) Molecular crystal packing model of πOF. (*D*) N_2 adsorption–desorption (red line, 77 K) and CO_2 (blue line, 273 K) adsorption isotherms of πOF. (*Inset*) The pore size distribution analysis based on the NLDFT model. (*E*) Energy-dispersive X-ray element mappings of πOFs. (*F*) PXRD patterns of recyclability test πOF. (*G*) Variable-temperature PXRD patterns of πOF. (*H*) Time-dependent PXRD patterns of πOF (after heat treatment at 240 °C) processed by (*I*) solvent annealing (methanol/chloroform).

method in $CHCl_3$ solution onto the SiO_2/Si substrates and evaluated the intrinsic charge transport properties of **πOF**. Optical microscope (OM) images and bright-field TEM images (top left inset) of the **πOF** microplates with a rhomboid shape and long-range regularity are presented in Fig. 3 *A* and *D*. The change in crystal intensities in the cross-polarized optical microscopy (CPOM) images indicate the single crystal nature of the microplates (Fig. 3 *B* and *C*). The out-of-plane XRD pattern with strong and sharp multiple Bragg diffractions in Fig. 3*E* indicate the high degree of crystallinity and highly ordered lamellar structure of **πOF** microplates. Two strong diffraction peaks at $2\theta = 5.41°$ and 10.74° are observed in the XRD analysis for the microplates (Fig. 3*E*), which could be assigned to (020) and (040) lattice planes, respectively, based on the data from the single-crystal structure. The corresponding selected area electron diffraction (SAED) patterns (Fig. 3*D*) of **πOF** microplates showed ordered and bright diffractions at different locations, indicating the single-crystal nature of the microplates. The SAED diffraction patterns of **πOF** are equal to a repeating period of 31.5 Å along one side of a rhomboid microplate direction and a repeating period of 21.1 Å along the other side of a rhomboid microplate, which can be assigned to the [100] and [103] directions based on prior single-crystal X-ray analysis. Besides, according to the law of consistency of interfacial angles, the measured interfacial angles of [100] direction and [103] direction from the images was 102.72°, which was equal to the calculated interfacial angles according to the single-crystal structure. The out-of-plane XRD data together with SAED pattern and single-crystal XRD data reveal that the **πOF** microplates are of the same phase as in the previously obtained single crystals. The field-effect transistor devices based on the rhomboid microcrystal of **πOF** were fabricated by an "organic ribbon mask" technique with four electrodes and channels to explore the directional charge transport properties (Fig. 3*F*) (29). The transfer and output characteristics of four different crystal planes tested under ambient conditions are shown in Fig. 3 *H* and *I* and *SI Appendix*, Fig. S5, and the mobility data are summarized in *SI Appendix*, Table S2. The OFET device based on **πOF** microplates show ambipolar characteristics, a concurrent existence of both hole (Fig. 3*H*) and electron (Fig. 3*I*) charge-carrier transport behavior. The same directional conducting channels, 1 ↔ 2 and 3 ↔ 4 or 2 ↔ 3 and 4 ↔ 1, show similar mobilities (square centimeters per volt per second) [$\mu_{h(1-2)} = 0.0705$, $\mu_{e(1-2)} = 0.26$, $\mu_{h(3-4)} = 0.089$, $\mu_{e(3-4)} = 0.27$, or $\mu_{h(2-3)} = 0.0676$, $\mu_{e(2-3)} = 0.12$, $\mu_{h(4-1)} = 0.0495$, $\mu_{e(4-1)} = 0.13$] (*SI Appendix*, Table S2). Also, the channels of 1 ↔ 2 and 3 ↔ 4 show higher mobility than the 2 ↔ 3 and 4 ↔ 1 channels. These results imply that the reticular quadrangular lattice of **πOF** possesses anisotropic properties, which are further studied using density functional theory (DFT) calculations.

Mechanistic Studies of Transport: From a Computational Perspective. We performed extensive theoretical calculations for the computational characterization of hole/electron transport in **πOF**. To be parallel to Fig. 3, we first focused on the packing along (100) and (103) planes, which rendered the π···π and x···x interactions, respectively (Fig. 4 *A* and *B*). First-principles calculations (*SI*

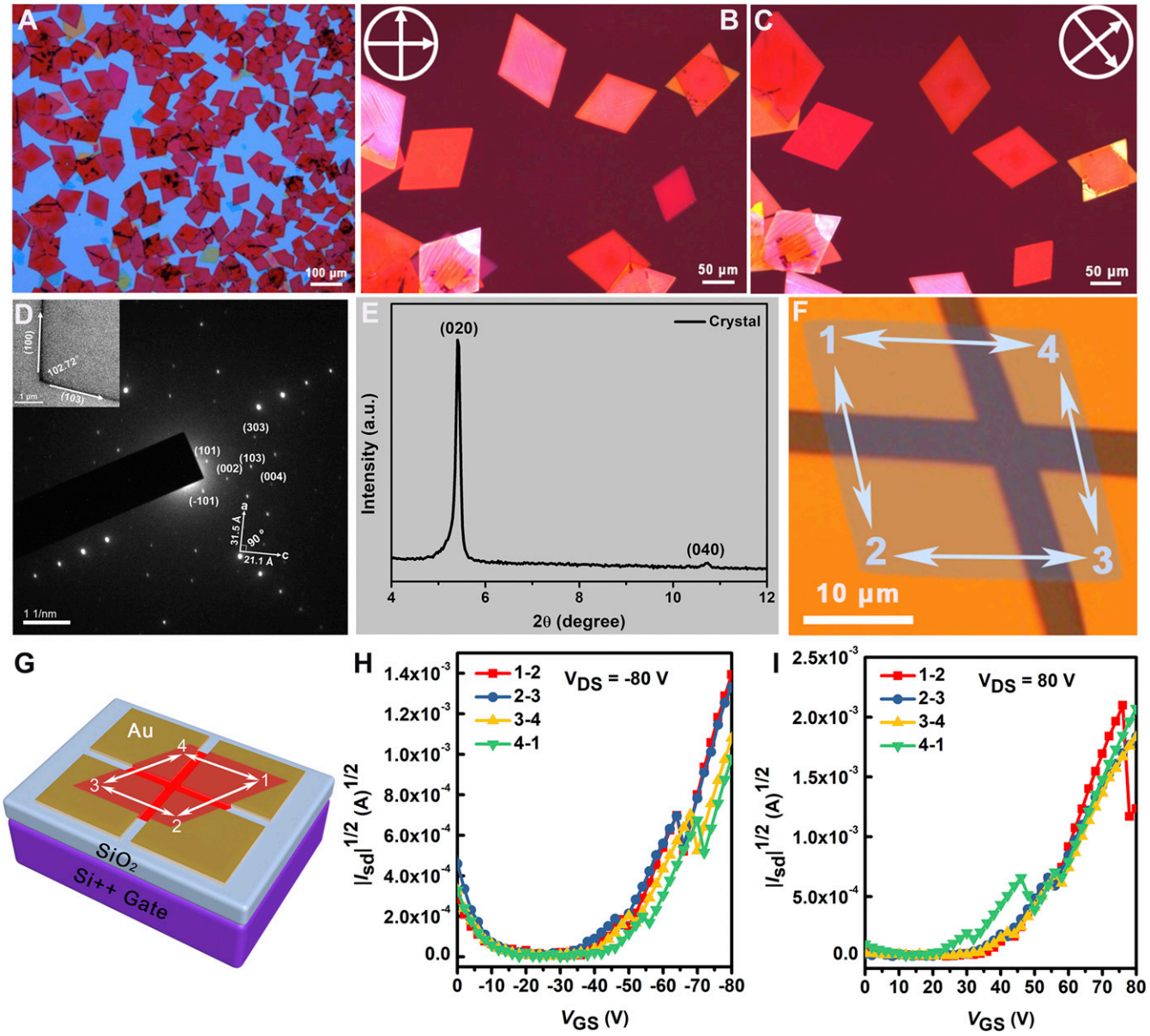

Fig. 3. Single-crystal transistor (OFET) characterization of πOF. (*A*) The OM image of **πOF** microplates [drop-casted in $CHCl_3$ (1 mg/mL)] self-assembled on SiO_2/Si substrate at room temperature. (*B* and *C*) CPOM images of the single-crystal microplates of **πOF**. (*D*) The TEM image and its corresponding SAED patterns. (*E*) One-dimensional out-of-plane XRD pattern of a single crystal data. (*F*) A transistor with four electrodes probing charge transport properties along different crystal planes. (*G*) The schematic diagram of **πOF** micro/nanocrystal transistor. (*H*) P-type and (*I*) N-type transfer characteristics of four OFET devices in different crystal planes.

Appendix, Fig. S6) revealed that the dimer binding energies and transfer integrals of π···π interactions are found to be considerably larger than those of x···x, due to relatively strong π···π binding. In the **πOF**, DFT calculated electron transfer integral (J_e) of π···π is more than a factor of four stronger than hole transfer integral (J_h), whereas J_h is conversely stronger than J_h in x···x (Fig. 4*B*). The intramolecular reorganization energies of hole (λ_h) and electron (λ_e) transfer are found to be the same (λ_h=λ_e = 82 meV) (see also *SI Appendix*, Fig. S6*B*). Transport calculations put forth that charge-carrier mobilities on the order of 1 cm^2/Vs can be achieved for a defect-free **πOF**. In addition, 1) $\mu_e > \mu_h$ over the π···π plane independent of the transport direction, attributed to $J_e > J_h$ along π···π and 2) electron mobility along (100) is roughly a factor of two larger than along (103) for both electron and hole mobilities, since transfer integrals along π···π are larger than those of x···x (e.g., 10.0 meV vs. 0.3 meV) (see also *SI Appendix*, Fig. S6*C*). Both 1 and 2 are very consistent with the OFET results in Fig. 3. Mobility calculations in the disordered phase (Fig. 4*D* and *SI Appendix*, Fig. S6*D*) show that the charge transport in **πOF** is susceptible against structural fluctuations arising from the thermal effects, attributed to the decreases in both hole and electron mobility relative to the crystal phase (Fig. 4*F*), even though directional mobility and $\mu_e > \mu_h$ are maintained. On the other hand, the mobilities along CH···π are much lower due to the lack of π···π interactions. The site-energy disorder of hole transport (Δ_h) and electron transport (Δ_e), arising from local charge–phonon coupling, are found to be similar and 60 meV (i.e., $\Delta_h \sim \Delta_e$ = 60 meV), as shown in *SI Appendix*, Fig. S6*E*, whereas the nonlocal electron–phonon coupling are larger than nonlocal hole–phonon coupling (see also Fig. 4*E*). Thus, computations suggest that the charge transport and

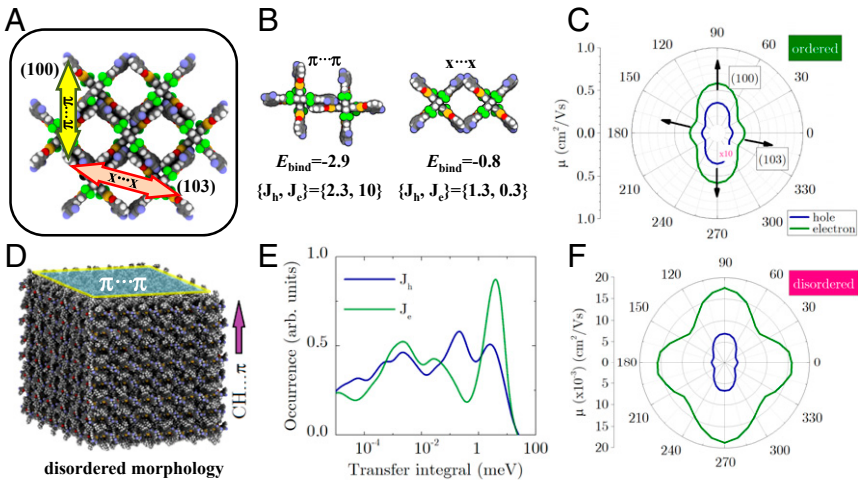

Fig. 4. Computational characterization of hole/electron transport. (*A*) Crystal packing. Green spheres represent alkyl chains. (*B*) Calculated binding energies (in electronvolts), hole transfer (J_e), and electron transfer integrals (J_e) (in millielectronvolts) (*C*) Direction-resolved hole and electron mobilities in ordered phase. (*D*) Atomistic morphology of the disordered phase. (*E*) Hole and electron transfer integral distributions in all transport directions. (*F*) Direction-resolved hole and electron mobilities in disordered phase.

mobility in **πOF** is mainly controlled by the intermolecular interactions, which emphasizes the significance of various interactions in the **πOF**.

Conclusion

In summary, we have developed a noncovalent π···π interaction-based organic framework (**πOF**). The 3D-ordered microporous structure that is connected via these kind of weak interactions presents not only supramaximal micropore and extremely high surface area but also an excellent stability and an ability to self-heal. It also shows remarkable transport properties in an OFET device, displaying distinct superiority compared to traditional COFs. The **πOF** not only extends the concept of porous molecular frameworks but also provides a direction toward applications of porous materials in organic electronics. Our study sheds light on a generation of microporous materials-based organic electronics allowing for strategic structural assembly for functionalities and even better performance in the future.

Materials and Methods

General Procedure for the Synthesis of SFIC. SF-CHO (100 mg, 0.048 mmol, 1 equivalent) and 2-(3-oxo-2,3-dihydro-1H-inden-1-ylidene) malononitrile (112 mg, 0.575 mmol, 12 equivalents) were dissolved in $CHCl_3$ (35 mL), then pyridine (1 mL) was added under argon. The mixture was then refluxed for 18 h, cooled to room temperature, poured into CH_3OH (200 mL), and filtered. The crude product was purified with column chromatography using hexane/dichloromethane (1:1) as eluent to obtain pure **SFIC** as a black solid (120 mg, 90%).

Transistor Device Fabrication and Characterization. The substrates were cleaned first with pure water, then piranha solution (H_2SO_4/H_2O_2 = 7:3), pure water, and finally with pure isopropyl alcohol and then blown dry with high-purity nitrogen gas. Micro/nanocrystals were formed using a dilute $CHCl_3$ solution (1 mg·mL^{-1}). Bottom-gate top-contact OFETs based on the micro/nanocrystals were constructed on an Si/SiO_2 substrate (n-type Si wafer containing 300-nm-thick SiO_2) using an "organic ribbon mask" technique. Prior to self-assembly of micro/nanocrystals, the Si/SiO_2 substrate was cleaned with pure *n*-hexane, pure chloroform, and pure isopropyl alcohol. Then, micro/nanocrystals were produced on Si/SiO_2 substrates through drop casting. Subsequently, 40-nm-thick source and drain electrodes were deposited on the micro/nanocrystals by thermal evaporation. Electrical characteristics of the devices were tested with a Keithley 4200-SCS semiconductor parameter analyzer and a Micromanipulator 6150 probe station in a glove box at room temperature. The mobilities were calculated from the saturation region with the following equation: $I_{DS} = (W/2L)\, C_i\mu\, (V_G - V_T)$ (2), where I_{DS} is the drain-source current, W is the channel width, L is the channel length, μ is the field-effect mobility, C_i is the capacitance per unit area of the gate dielectric layer, and V_G and V_T are the gate voltage and threshold voltage, respectively. This equation defines the important characteristics of electron mobility (μ), on/off ratio ($I_{on/off}$), and threshold voltage (V_T), which could be deduced from the equation using the current–voltage plot.

Data and Materials Availability. All data are available in the main text and in *SI Appendix*. Crystallographic parameters for the structure of **πOF** (*SI Appendix*) are archived at the Cambridge Crystallographic Data Centre (https://www.ccdc.cam.ac.uk/) under reference number CCDC 1894479.

ACKNOWLEDGMENTS. Y.Y. acknowledges University of California, Los Angeles unrestricted grant 442551-Y.Y.-41292. J.L.Y. acknowledges the work was done while he was an undergraduate student in Prof. Christopher Chang's group at the University of California, Berkeley. We gratefully thank Ms. Danlei Zhu, Institute of Chemistry, Chinese Academy of Sciences, for assistance with the OFET device.

1. Y. Wang *et al.*, Organic crystalline materials in flexible electronics. *Chem. Soc. Rev.* **48**, 1492–1530 (2019).
2. X. Chen, J. A. Rogers, S. P. Lacour, W. Hu, D. H. Kim, Materials chemistry in flexible electronics. *Chem. Soc. Rev.* **48**, 1431–1433 (2019).
3. S. Kwon *et al.*, Recent progress of fiber shaped lighting devices for smart display applications-a fibertronic perspective. *Adv. Mater.* **32**, e1903488 (2020).
4. D. Meng *et al.*, High-performance solution-processed non-fullerene organic solar cells based on selenophene-containing perylene bisimide acceptor. *J. Am. Chem. Soc.* **138**, 375–380 (2016).
5. D. Meng *et al.*, Three-bladed rylene propellers with three-dimensional network assembly for organic electronics. *J. Am. Chem. Soc.* **138**, 10184–10190 (2016).
6. G. Zhang *et al.*, Nonfullerene acceptor molecules for bulk heterojunction organic solar cells. *Chem. Rev.* **118**, 3447–3507 (2018).
7. P. Cheng, G. Li, X. Zhan, Y. Yang, Next-generation organic photovoltaics based on non-fullerene acceptors. *Nat. Photonics* **12**, 131–142 (2018).
8. A. L. Briseno *et al.*, Patterning organic single-crystal transistor arrays. *Nature* **444**, 913–917 (2006).
9. S. W. Thomas 3rd, G. D. Joly, T. M. Swager, Chemical sensors based on amplifying fluorescent conjugated polymers. *Chem. Rev.* **107**, 1339–1386 (2007).
10. H. Li *et al.*, Monolayer two-dimensional molecular crystals for an ultrasensitive OFET-based chemical sensor. *Angew. Chem. Int. Ed. Engl.* **59**, 4380–4384 (2020).
11. K. Müllen, U. Scherf, *Organic Light Emitting Devices: Synthesis, Properties and Applications*, (Wiley-VCH, 2006).
12. M. Calik *et al.*, Extraction of photogenerated electrons and holes from a covalent organic framework integrated heterojunction. *J. Am. Chem. Soc.* **136**, 17802–17807 (2014).
13. J. Jiang, Y. Zhao, O. M. Yaghi, Covalent chemistry beyond molecules. *J. Am. Chem. Soc.* **138**, 3255–3265 (2016).
14. A. P. Côté *et al.*, Porous, crystalline, covalent organic frameworks. *Science* **310**, 1166–1170 (2005).

15. N. Huang, P. Wang, D. Jiang, Covalent organic frameworks: A materials platform for structural and functional designs. *Nat. Rev. Mater.* **1**, 16068 (2016).
16. J.-H. Deng *et al.*, π-π stacking interactions: Non-negligible forces for stabilizing porous supramolecular frameworks. *Sci. Adv.* **6**, eaax9976 (2020).
17. P. Sozzani, A. Comotti, S. Bracco, R. Simonutti, A family of supramolecular frameworks of polyconjugated molecules hosted in aromatic nanochannels. *Angew. Chem. Int. Ed. Engl.* **43**, 2792–2797 (2004).
18. Y.-Y. Lyu *et al.*, Highly efficient red phosphorescent OLEDs based on non-conjugated silicon-cored spirobifluorene derivative doped with Ir-complexes. *Adv. Funct. Mater.* **19**, 420–427 (2009).
19. N. Qiu *et al.*, Nonfullerene small molecular acceptors with a three-dimensional (3D) structure for organic solar cells. *Chem. Mater.* **28**, 6770–6778 (2016).
20. D. Heredia *et al.*, Spirobifluorene-bridged donor/acceptor dye for organic dye-sensitized solar cells. *Org. Lett.* **12**, 12–15 (2010).
21. G. Han, Y. Guo, L. Ning, Y. Yi, Improving the electron mobility of ITIC by end-group modulation: The role of fluorination and π-extension. *Sol. RRL.* **3**, 1800251 (2019).
22. Y. Lin *et al.*, An electron acceptor challenging fullerenes for efficient polymer solar cells. *Adv. Mater.* **27**, 1170–1174 (2015).
23. G. Han, Y. Yi, Z. Shuai, From molecular packing structures to electronic processes: Theoretical simulations for organic solar cells. *Adv. Energy Mater.* **8**, 1702743 (2018).
24. C. G. Bezzu, M. Helliwell, J. E. Warren, D. R. Allan, N. B. McKeown, Heme-like coordination chemistry within nanoporous molecular crystals. *Science* **327**, 1627–1630 (2010).
25. K. J. Msayib *et al.*, Nitrogen and hydrogen adsorption by an organic microporous crystal. *Angew. Chem. Int. Ed. Engl.* **48**, 3273–3277 (2009).
26. Y. Chen, A. M. Kushner, G. A. Williams, Z. Guan, Multiphase design of autonomic self-healing thermoplastic elastomers. *Nat. Chem.* **4**, 467–472 (2012).
27. H. Yamagishi *et al.*, Self-assembly of lattices with high structural complexity from a geometrically simple molecule. *Science* **361**, 1242–1246 (2018).
28. P. Cordier, F. Tournilhac, C. Soulié-Ziakovic, L. Leibler, Self-healing and thermoreversible rubber from supramolecular assembly. *Nature* **451**, 977–980 (2008).
29. L. Jiang *et al.*, Organic single-crystalline ribbons of a rigid "H"-type anthracene derivative and high-performance, short-channel field-effect transistors of individual micro/nanometer-sized ribbons fabricated by an "organic ribbon mask" technique. *Adv. Mater.* **20**, 2735–2740 (2008).